

Article

# Petrogenesis of the Microgranular Enclaves and Their Host Granites from the Xitian Intrusion in South China: Implications for Geodynamic Setting and Mineralization

Miao He \*, Qing Liu \*, Quanlin Hou, Jinfeng Sun and Quanren Yan

CAS Key Laboratory of Computational Geodynamics, College of Earth and Planetary Sciences, University of Chinese Academy of Sciences, Beijing 100049, China; quhou@ucas.ac.cn (Q.H.); sjf@ucas.ac.cn (J.S.); qryan@ucas.ac.cn (Q.Y.)

\* Correspondence: hemiao@ucas.ac.cn (M.H.); qingliu@ucas.ac.cn (Q.L.)

Received: 21 September 2020; Accepted: 23 November 2020; Published: 26 November 2020



**Abstract:** The South China Block had experienced a significant tectonic transition during the Mesozoic in response to the subduction of the Paleo- and the Pacific Ocean. Large-scale granitic intrusions with massive mineralization are widespread in South China, and their tectonic settings are not defined. The Xitian intrusion is ideal for probing the geodynamic setting and mineralization in South China because they comprise an abundance of microgranular enclaves (MEs) and diverse types of granite associated with mineralization. Age determined by zircon U-Pb dating suggests that the MEs and their host granites are coeval within error, of ca. 152 Ma. The MEs have a similar initial Hf-O isotopic composition as host granites, and the rapid cooling mineral textures indicate that they are autoliths. Geochemical data show that the host granites are high-K, calc-alkaline, and transitional from metaluminous to peraluminous, slightly enriched in light rare earth elements (LREEs) relative to heavy rare earth elements (HREEs), with obvious negative Eu anomalies, belonging to I-type. The Nb/Ta and Zr/Hf ratios indicate the volatile penetrates the magmatic-forming process, and the fluid with abundant volatile could extract metal element effectively from the mantle.

**Keywords:** microgranular enclaves; zircon geochronology; Hf-O isotopes; South China

## 1. Introduction

The South China Block in the southwestern part of the Circum-Pacific tectonic domain consists of the Cathaysia Block in the southeast and the Yangtze Block in the northwest. It is characterized by the extensive occurrence of granites, associated with numerous world-famous polymetallic deposits [1–3]. The origin of large-scale intrusions was commonly associated with mantle magmatism [4,5]. MEs (including mafic and intermediate microgranular) are common in volcanic and plutonic rocks in South China [6,7]. They were interpreted as globules of the mantle- and crust-mantle derived magma [8–10]. These enclaves can tend to equalize their composition with host rocks during hybridization [11]. The mixing of the mantle and crustal magmas at different levels can mark the transition from crustal to mixed granites [12]. Nevertheless, the origin of MEs has been interpreted to restite fragments that have been transported from the source region of the magma [13,14] or as the result of the accumulation of early crystals trapped within its residual liquid at emplacement pressures [15–18]. Evidently, the origin of enclaves in granitic intrusions has a key role in indicating magma differentiation mechanism [19].

The South China Block had experienced multiple tectonothermal events during the Mesozoic. As a result, widespread Mesozoic granites were formed accompanied by a series of large W-Sn

deposits [3,20,21]. However, whether the mantle was involved in metallogenic magmatism is still debated [2,22,23]. In this paper, the MEs provide geological evidence of a genetic link with their host rocks. A detailed investigation of the petrography, zircon U-Pb geochronology, geochemistry, zircon Hf-O isotopes was carried out on the MEs and the host granites from the Xitian intrusion. This research aims to identify the petrogenesis of granitoids, the origin of mineralization, and to reveal the geodynamics setting and mineralization of magmatism.

## 2. Geological Setting

The Xitian intrusion is located in the central part of the Nanling Range, accompanied by tin-polymetallic deposits [24]. Nanling Range is one of the world's most important magmatic-hydrothermal W-Sn provinces (Figure 1) [25–27]. It contains widely distributed granites and numerous W-Sn deposits, including Shizuyuan, Furong, Taoxikeng, Da'ao, Xihuashan, and Guposhan (Figure 1) [1–3,22].

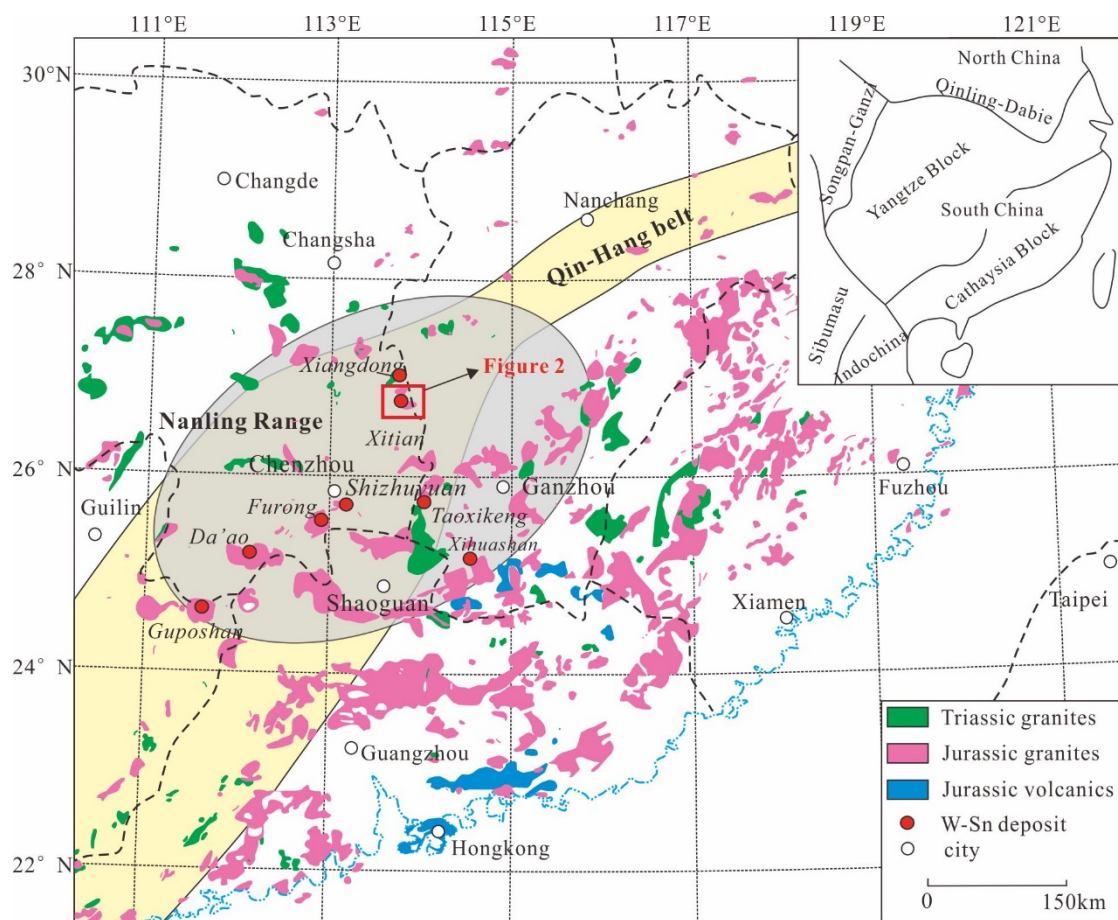


**Figure 1.** Geological sketch map of the South China Block showing the distribution of Mesozoic granite-volcanic rocks. The locations of granites and volcanics refer to [28].

The Xitian deposit also belongs to the Qin-Hang belt, an economic ore belt in South China [3,23]. It is a Neoproterozoic suture belt result from the collisions of the Yangtze Block and the Cathaysia Block, along the Jiangshan-Shaoxing fault [24,28]. Numerous Middle to Late Jurassic (171–150 Ma) calc-alkaline granitoids rocks and related Cu-Au-Mo-Pb-Zn-W-Sn deposits are distributed along the Qin-Hang belt in response to the Jurassic Paleo-Pacific Plate subduction [29,30]. Because of the superimposed influence of multistage tectonmagmatic events, the source of magma associated with polymetallic deposits remains highly controversial.

In this region, the stratigraphical sequences consist of the Palaeozoic to Early Proterozoic clastic rocks, Mesozoic carbonate, and clastic rocks, partly unconformable overlain by Neogene clay rocks (Figure 2). The intensive folding and deformed basement are mainly composed of weakly metamorphosed clastic sedimentary rocks in Sinian to Silurian. Overlying upper Jurassic to Cretaceous sedimentary rocks are mostly sandstones deposited in rift basin [31].

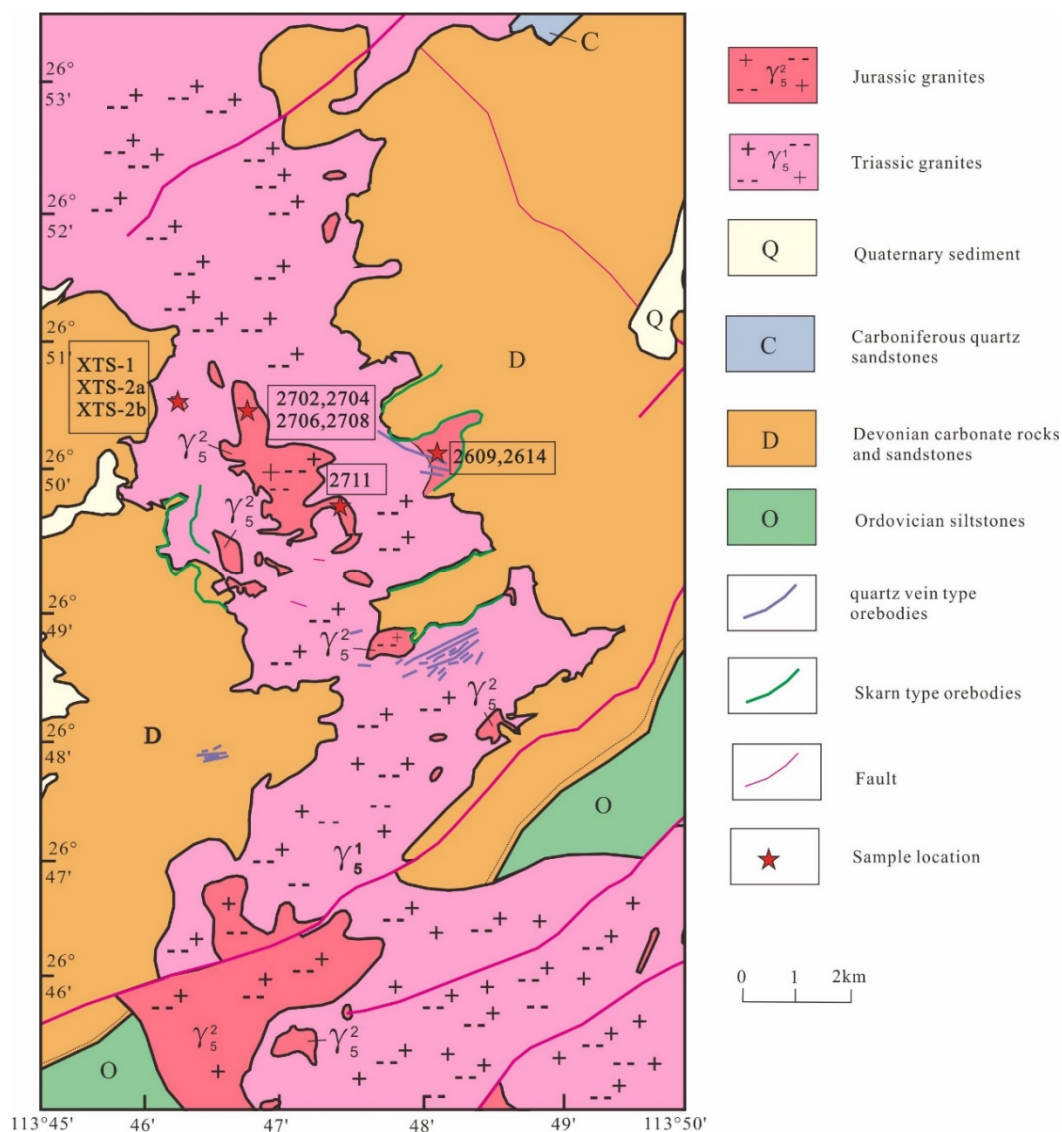
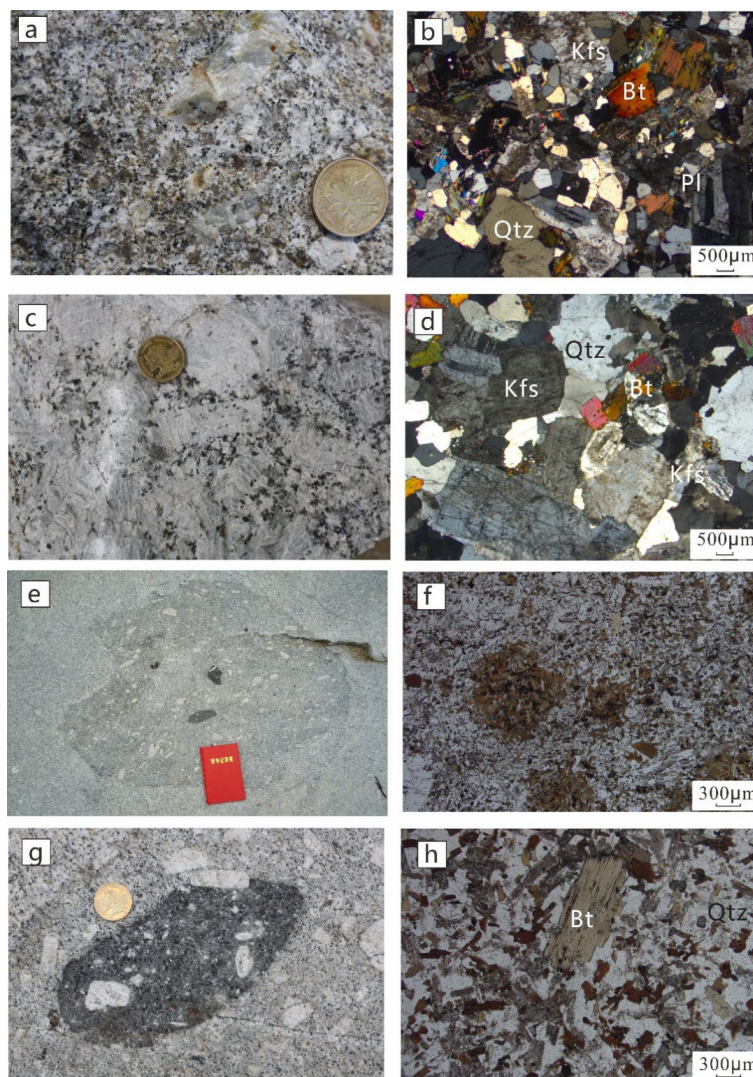


Figure 2. Geological sketch map of the Xitian ore field (modified after [32]).

The Xitian intrusion is dumbbell-shaped and mainly occurred in two episodes: the Late Triassic (ca. 230 Ma) and the Late Jurassic (ca. 150 Ma) [24,32–37]. The Triassic plutons occurred as the batholiths intruded into Ordovician rocks and Devonian carbonate rocks. The Late Jurassic granites are scattered and intruded into the older Triassic plutons. They are mainly distributed in the interior of the pluton and along the eastern orebody (Figure 2). The two tectonic events accompanying large-scale magmatic activity result in the E-W trending and NE trending structures [36]. The Xitian ore field developed a series of symmetrical high-angle normal faults, as the bounding faults of Chahan rift basin [37,38]. The metallogenic magmatism mainly explodes in 175–150 Ma [22,27]. The ore veins mainly occurred in the contact zone between the granite and Devonian carbonate rocks. It is obvious that the faults control the ore veins in the area [39]. Tungsten is chiefly hosted in wolframite and scheelite, and tin is mainly in cassiterite. The ore veins of the W-Sn deposit are mainly distributed as veinlet-disseminated [22,38].

### 3. Petrography

The Xitian intrusion mainly consists of biotite granite and biotite monzogranite (Figure 3a–d). The biotite granite consists of quartz (35–40 vol.%), K-feldspar (30–36 vol.%), plagioclase (20–25 vol.%), biotite (5–7 vol.%), with granitic texture (Figure 3b). The biotite monzogranite is characterized by 10–15 vol.% megacrysts composed mainly of K-feldspar and matrix containing 30–35 vol.% quartz, 30–35 vol.% K-feldspar, 25–30 vol.% plagioclase, 5–6 vol.% biotite (Figure 3d). The dark microgranular enclaves were discovered in both types of the late Jurassic granite. They are rounded-spheroid and scattered spot-like, with a plastic shape (Figure 3e). Biotite is gathered to cluster (Figure 3f), while large feldspar crystallized at the contact zone of MEs and granites (Figure 3g). The mineral compositions are quite similar to those of the host granites (Figure 3h).



**Figure 3.** Field photographs and microscope images of rocks and microgranular enclaves (MEs) of the Xitian intrusion. (a,b) Biotite monzogranite; (c,d) Biotite granite; (e) Field photograph showing MEs in the granite of the Xitian intrusion; (f) Biotite agglomerates; (g) The feldspar crystal passes through MEs; (h) MEs. Abbreviations: Qtz (quartz); Kfs (K-feldspar); Pl (plagioclase); Bt (biotite).

### 4. Sampling and Analytical Methods

After the petrographic study, eleven fresh and representative rocks were crushed and powdered (<200 mesh) for geochemical study. Four samples (2708, 2614, 2711, and 2713) were classified as biotite

granite, while four samples (2609, 2706, 2702, and 2704) represent biotite monzogranite. Both types were collected from the margin to the central parts of the pluton. For in situ geochronology analysis, two samples of the host granites (2706 and 2708) and two samples of the microgranular enclaves (XTS-1 and XTS-2b) were collected. Sampling locations were shown in Figure 2.

#### 4.1. Zircon U-Pb Dating by SIMS and LA-ICP-MS

Zircons for U-Pb analysis were separated by using conventional magnetic and density techniques. The sample and standards were put together into epoxy, which was then polished to section the crystals in half. In order to reveal their internal structures and target sites for U-Pb dating, all zircons were documented with transmitted and reflected light micrographs as well as cathodoluminescence (CL) images.

U, Th, and Pb of zircons (2706 and 2708) were measured using the Cameca IMS-1280 secondary ion mass spectrometry (SIMS) at the Institute of Geology and Geophysics, Chinese Academy of Sciences in Beijing (IGGCAS). The mount was vacuum-coated with high-purity gold before analysis. U-Th-Pb isotopic ratios and absolute abundances were determined relative to the standard zircons Plešovice [40], interspersed with those of the unknown grains. The  $O_2^-$  primary ion beam with an intensity of ca. 10 nA was accelerated at  $-13$  kV. A single electron multiplier was used on ion-counting mode to measure the secondary ion beam intensities by peak jumping sequence [41]. Measured compositions were calibrated of common Pb using non-radiogenic  $^{204}Pb$ . An average of present-day crustal composition [42] was used for the common Pb correction. Data reduction was carried out using the Isoplot program [43].

Zircons used for laser inductively coupled plasma mass spectrometry (LA-ICP-MS) U-Pb dating of samples (XTS-1 and XTS-2b) were conducted using an Agilent 7500a ICP-MS equipped with a 193 nm GeoLas laser at IGGCAS. The analysis parameters and detailed procedures are described by [44]. The reference material (NIST 610) and internal calibrant ( $^{29}Si$ ) were used to calibrate the U, Th, and Pb concentrations. The  $^{207}Pb/^{206}Pb$  and  $^{206}Pb/^{238}U$  ratios were calculated using the GLITTER program. Data were corrected using the standard zircon (91500) as an external calibrant, with a standardization error of  $\sim\pm 1\%$  (circa 16 Ma). Because the  $^{204}Pb$  isotope cannot be precisely measured, common Pb contents were evaluated using the method described by [45]. The age was calculated and plotted using ISOPLOT by omitting highly discordant and compositionally anomalous data [43]. Age uncertainties are reported for precision and including a 1% standardization error. Unless otherwise specified, all errors are reported at  $2\sigma$  confidence [46].

#### 4.2. Whole-Rock Major and Trace Elements

For major-element analyses, samples with fluorescent agents were mixed and fused into glass disks. Whole-rock major element analysis was done by X-ray fluorescence (XRF-1500) at the IGGCAS, with an analytical precision better than 1%. Standard GSR-3 was used to monitor the analytical accuracy. Trace element concentrations were determined by ICP-MS on a solution basis, using the techniques described by [47]. An internal standard Rh solution monitored counting signal drift. According to duplicate analyses on these standards, the precision is generally better than 5% for most trace elements.

#### 4.3. In Situ Zircon Hf and O Isotopes Analysis

In situ zircon oxygen isotopes were also conducted using the same Cameca ion microprobe at IGGCAS. Isotopes  $^{16}O$  and  $^{18}O$  were collected simultaneously using Faraday cups. The instrumental mass fraction factor (IMF) was corrected using standard zircon Penglai. Measured  $^{16}O/^{18}O$  ratios were normalized using Vienna Standard Mean Water composition (VSMOW,  $^{16}O/^{18}O = 0.0020052$ ). The detailed analytical procedures were similar to those described by [44].

After the oxygen isotopic analyses, the sample mountings' conductive coatings were removed, but the grains were not repolished, leaving the analyzed spots visible to guide the Hf analyses. Zircon Hf isotope analyses were conducted by MC-ICP-MS using a Neptune system. The detailed analytical

procedure and correction for interferences were followed as that described by [48]. During analysis, the  $^{176}\text{Hf}/^{177}\text{Hf}$  ratio of the standard zircon GJ-1 was  $0.2820217 \pm 1.3$  ( $2\sigma$ ,  $n = 21$ ), similar to the commonly accepted  $^{176}\text{Hf}/^{177}\text{Hf}$  ratio of  $0.281999 \pm 8$  ( $2\sigma$ ,  $n = 10$ ) measured using the solution method. The zircon Hf isotopic compositions of the granites (the initial  $^{176}\text{Hf}/^{177}\text{Hf}$  ratio for each spot) were calculated using the U-Pb crystallization date of the grain or the weighted mean age of the host granite. The age-corrected  $^{176}\text{Hf}/^{177}\text{Hf}$  ratio was then expressed as  $\epsilon_{\text{Hf}}(t)$ , calculated using the parameters of  $^{176}\text{Hf}/^{177}\text{Hf} = 0.282785$  and  $^{176}\text{Lu}/^{177}\text{Hf} = 0.0336$  [49].

## 5. Analytical Results

### 5.1. Zircon U-Pb Ages

Zircon grains from the biotite granite and biotite monzogranite are colorless and transparent, behaving homogeneous and compositionally zoning in CL images (Figure 4). They are euhedral, prisms, and pyramids in shape, ranging from 80 to 250  $\mu\text{m}$  in length. Concentric oscillatory zonings are generally developed in zircon grains, whose cores exhibit segments with sector zoning. Only a few zircon grains contain ovoid cores. Others show typical oscillatory zoning without inherited cores. Zircons in Xitian granites have variable Th (124–3650 ppm) and U (209–3596 ppm) contents, with Th/U ratios of 0.1–1.7. All these characteristics suggest that these zircons are magmatic in origin [50–52]. The analytical results of zircon U-Pb dating are summarized in Supplementary Table S1. Despite the captured and inherited crystals, zircon grains (2706) from the biotite monzogranite yield a weighted mean  $^{206}\text{Pb}/^{238}\text{U}$  age of  $150.5 \pm 1.1$  Ma (MSWD = 0.95, Figure 5). For the Xitian intrusion, samples of the biotite granite (2708) give a weighted mean  $^{206}\text{Pb}/^{238}\text{U}$  age of  $151.3 \pm 1.8$  Ma (MSWD = 1.6, Figure 5), which is the best estimate of the magma crystallization time.

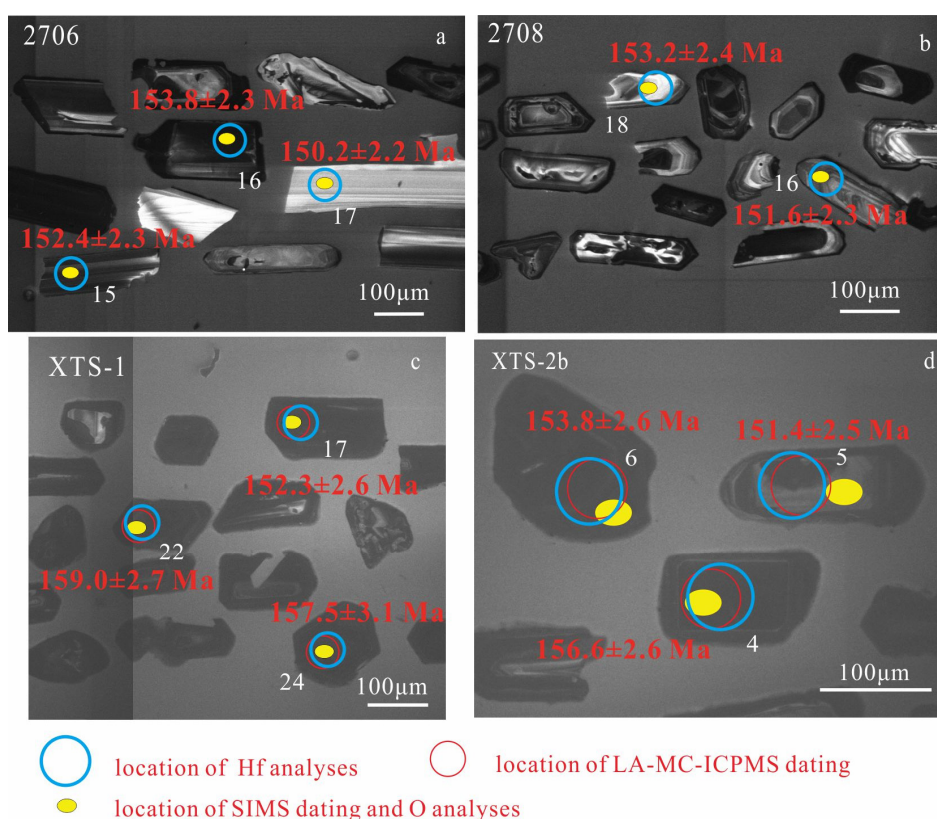


**Figure 4.** Cathodoluminescence (CL) images of representative zircons from (a) biotite monzogranite, (b) biotite granite, and (c,d) microgranular enclaves. The circles show the locations of in situ U-Pb, Hf, and O isotopes analyses.

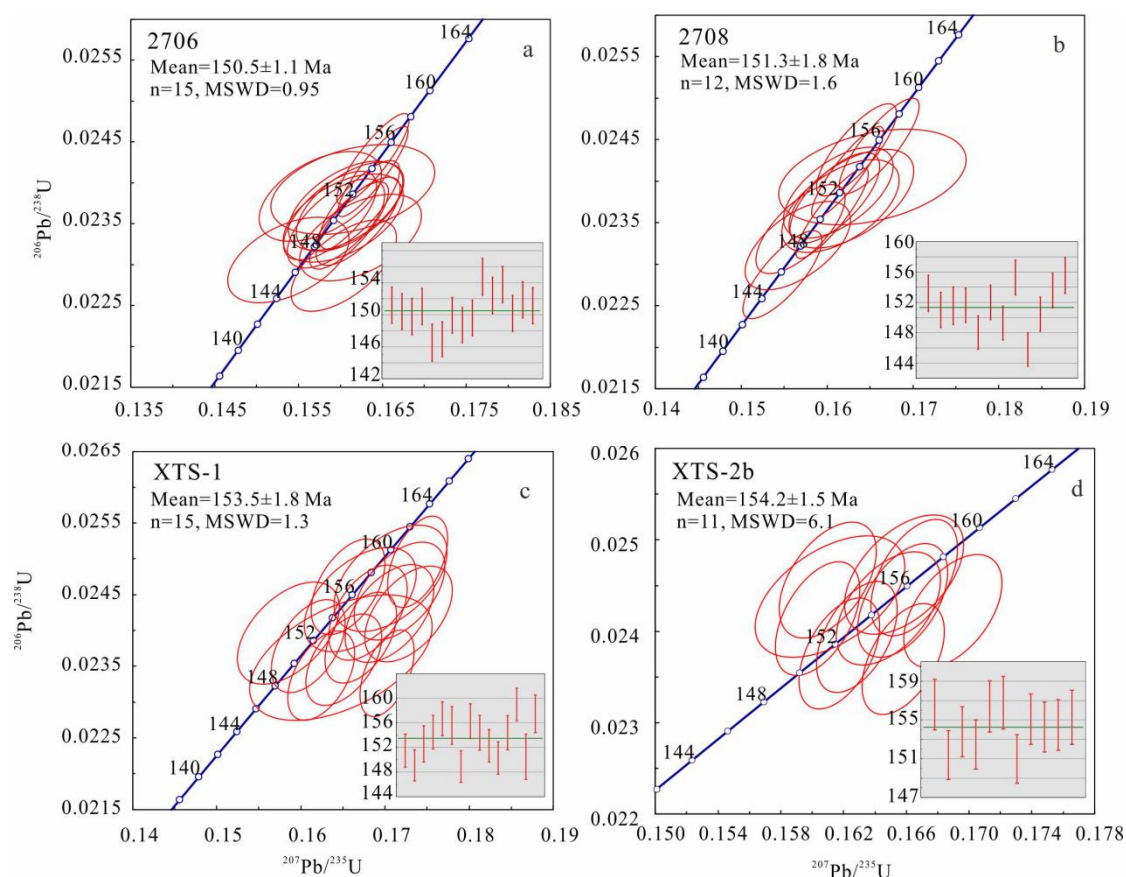


**Figure 5.** Zircon U-Pb ages of the host granites (a,b) and MEs (c,d) from the Xitian intrusion.

Zircon grains from microgranular enclaves are stubby to prismatic, whose lengths range from 100 to 200  $\mu\text{m}$  with length/width ratios of 1.1–1.5. They have variable Th/U ratios ( $\text{Th}/\text{U} = 0.1\text{--}1.2$ ). In general, these zircons are brown or colorless and have a few snatchy cracks in their crystals, suggesting a magmatic origin [50–52]. The analytical results of zircon U-Pb dating are summarized in Supplementary Table S2. Fifteen spots analyses of sample (XTS-1) plot close to the Concordia curve (Figure 5) and yield a weighted mean age of  $153.5 \pm 1.8$  Ma (MSWD = 1.3). In addition, the remaining 11 spots analyses of XTS-2b yield a weighted mean  $^{206}\text{Pb}/^{238}\text{U}$  ages of  $154.2 \pm 1.5$  Ma (MSWD = 6.1), which is interpreted as the best estimate of the crystallization age (Figure 5). The ages within analytical error suggest that the host granites and microgranular from the Xitian intrusion are coeval within the error.

## 5.2. Whole-Rock Major and Trace Element

Based on the whole-rock major element result (Supplementary Table S3), the biotite granites and biotite monzogranite from the Xitian intrusion are weakly peraluminous with A/CNK (molar ratios  $\text{Al}_2\text{O}_3/[\text{CaO} + \text{Na}_2\text{O} + \text{K}_2\text{O}]$ ) index values around 1.1, belonging to the high-K calc-alkaline series (Figure 6). They exhibit high  $\text{SiO}_2$  (70.6–77.9 wt.%), slightly high  $\text{K}_2\text{O}$  (3.9–5.6 wt.%), and constant  $\text{Na}_2\text{O}$  (3.0 to 4.0 wt.%). They contain  $\text{Al}_2\text{O}_3$  varying from 12.2–14.2 wt.% and low CaO contents (0.6–1.6 wt.%). MEs are intermediate to felsic in composition (Figure 6a) and exhibit variable  $\text{SiO}_2$  from 59.0 wt.% to 72.0 wt.%. Their A/CNK values range from 0.95–1.98 (Figure 6a). These MEs have low and variable MgO (0.09–0.17 wt.%) and relatively low  $\text{TFe}_2\text{O}_3$  values varying from 0.23–0.52 wt.%. The host granites have significantly higher  $\text{K}_2\text{O}$  contents than MEs (Supplementary Table S3). Consequently, these granites and monzogranites are similar to the shoshonitic series (Figure 6b). In the Harker diagrams, host granites (biotite monzogranite and biotite granite) and microgranular enclaves define

broadly linear trends. Their CaO, Al<sub>2</sub>O<sub>3</sub>, TiO<sub>2</sub>, and P<sub>2</sub>O<sub>5</sub> contents decrease with increasing SiO<sub>2</sub> contents (Figure 7).

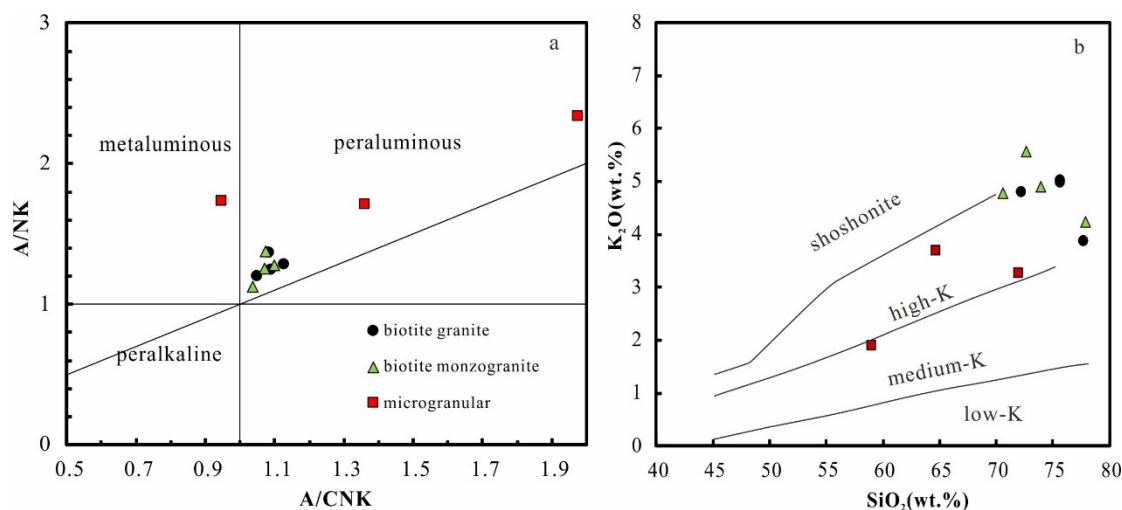


**Figure 6.** (a) A/CNK vs. A/NK diagram [53]; (b) SiO<sub>2</sub> vs. K<sub>2</sub>O diagram (solid lines from [54]).

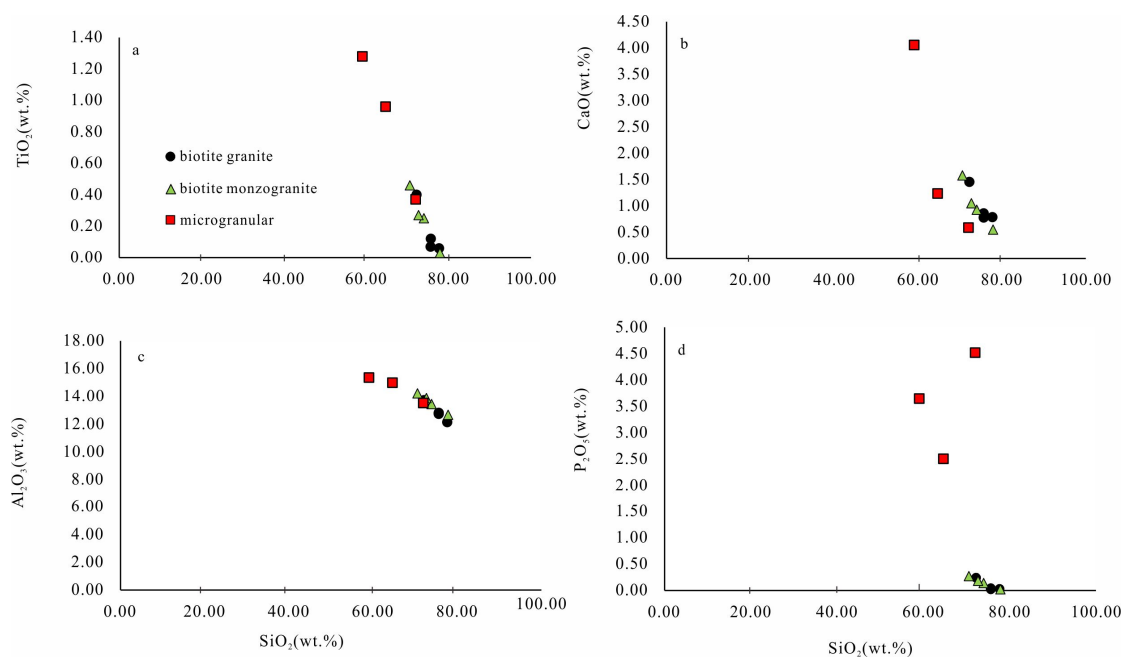


**Figure 7.** Harker diagrams showing a variation of selected major oxides (e.g., TiO<sub>2</sub> (a), CaO (b), Al<sub>2</sub>O<sub>3</sub> (c), P<sub>2</sub>O<sub>5</sub> (d)) versus SiO<sub>2</sub> in the Xitian intrusion.

Primitive mantle-normalized trace element patterns for granites and MEs show the enrichments in Rb, Th, and U and depletions in Ba, Sr, Eu, and Nb (Figure 8a). Therefore, they both have high Rb/Sr (4.1–39.6) and Rb/Ba (1.2–29.6). Chondrite-normalized REE patterns (Figure 8b) for the biotite granites and biotite monzogranite show a different enrichment of heavy rare earth elements (HREEs). Both host granites and MEs are rich in LREE with Eu negative anomaly ( $\sigma\text{Eu} = 0.007\text{--}0.146$ ). The MEs and some granites show a smaller Eu anomaly and a minor amount of HREE. The detailed trace element data from the Xitian intrusion are listed in Supplementary Table S4.

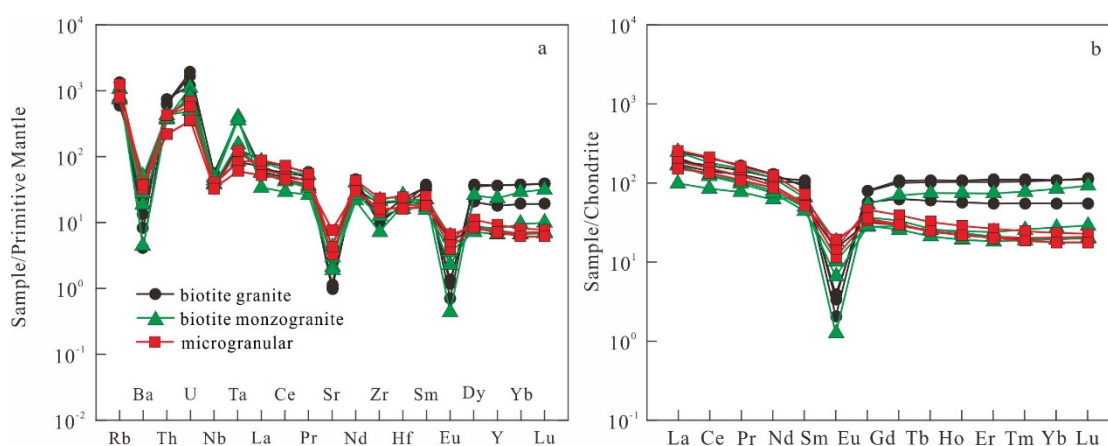


**Figure 8.** (a) Primitive-normalized trace element spider diagram of the Xitian intrusion; (b) Chondrite-normalized REE patterns for the Xitian intrusion. Normalized values are from [55].

### 5.3. Zircon Hf and O Isotopes

Five samples, including two biotite monzogranite (2609 and 2706), one biotite granite (2708), and their microgranular enclave (XTS-1 and XTS-2b), were chosen for zircon Hf and O isotopic analysis using LA-ICP-MS and SIMS, respectively. Another five samples, including two biotite monzogranite (2702 and 2704) and three biotite granites (2614, 2711, and 2713), were selected for zircon Hf isotopic analysis. The results are shown in Supplementary Table S5.

Hf isotope analyses were conducted on zircon grains that were previously analyzed for U-Pb dating. Zircons from the MEs have similar Hf isotopic compositions compared with the host biotite granites (Figure 9). Most of the analyzed zircon grains show low  $^{176}\text{Lu}/^{177}\text{Hf}$  ratios ( $<0.002$ ); thus, the analytical  $^{176}\text{Hf}/^{177}\text{Hf}$  ratios can be used to represent the isotopic compositions of magmas at the time of formation [48]. The dated at about 150 Ma magmatic zircons from MEs samples (XTS-1 and XTS-2b) have  $^{176}\text{Hf}/^{177}\text{Hf}$  ratios ranging from 0.282448 to 0.282600, corresponding to  $\varepsilon_{\text{Hf}}(t)$  values from  $-8.16$  to  $-2.93$  (average of  $-5.61$ ). Zircons from the granites (samples 2609, 2706, 2702, 2704, 2708, 2614, 2711, and 2713) have variable Hf isotopic compositions with  $\varepsilon_{\text{Hf}}(t)$  values ranging from  $-9.08$  to  $0.32$  (average of  $-6.19$ ). The granites and MEs have two-stage Hf model age ( $T_{\text{DM}2}$ ) values of  $1.18$ – $1.78$  Ga and  $1.39$ – $1.72$  Ga, respectively. Three grains have the  $\varepsilon_{\text{Hf}}(t)$  values around zero, indicating mantle involvement in their genesis. Zircons from the MEs have similar O isotopic compositions compared with the host granites (Figure 9). Zircons from the MEs (samples XTS-1 and XTS-2b) have O isotopic compositions with  $\delta^{18}\text{O}$  values ranging from  $8.4\text{‰}$  to  $9.3\text{‰}$ . Eighteen spot analyses were performed on the biotite monzogranite (2609), yielding  $\delta^{18}\text{O}$  values from  $8.6\text{‰}$  to  $9.4\text{‰}$ . Fifteen-spot analyses were performed on the granites (2706), yielding  $\delta^{18}\text{O}$  values from  $8.4\text{‰}$  to  $9.5\text{‰}$ . Zircon grains from biotite granites (2708) have similar  $\delta^{18}\text{O}$  values from  $8.1\text{‰}$  to  $9.2\text{‰}$ . The indistinguishable Lu-Hf and O isotope compositions between biotite granites and biotite monzogranites further confirm their genetic relation. Moreover, both zircon grains of MEs and host granites have similar Lu-Hf isotope compositions, indicating their parental magmas are from the same source.

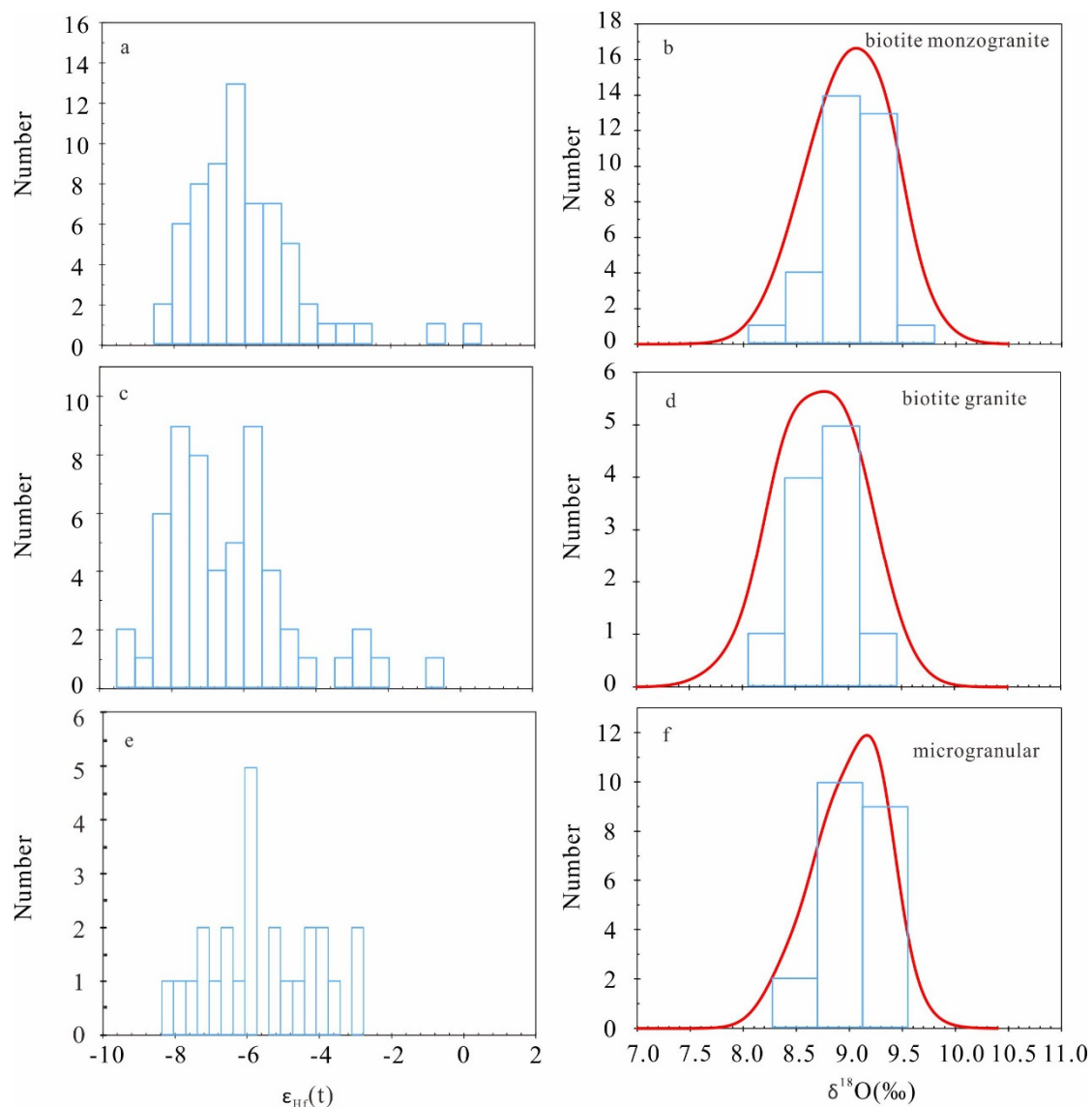


**Figure 9.** The histogram of  $\epsilon_{\text{Hf}}(t)$  (a,c,d) and  $\delta^{18}\text{O}$  values (b,e,f) from the Xitian intrusion and MEs.

## 6. Discussion

### 6.1. Origin of the MEs

Igneous microgranular enclaves are widespread in granitic rocks and point to magma mixing processes [56]. However, enclaves are common in granitic rocks, and their presence should not be used to infer any particular tectonic setting [57] specifically. Nevertheless, there are considerable models proposed to decipher the origins of MEs, for instance, whether they are restites of source rocks [13,14], autoliths [58,59], or they were formed by the mantle-crust magma mixing [12,60].

In general, restite is entrained by a partial melt and is considered to represent the magmatically equilibrated source material [13]. The chemical composition of restite is usually complementary to the melt component in the host magma. The xenolith is formed from an older melting event and often has magmatic reaction textures [60]. The MEs and their host granites show similar zircon U-Pb ages of ca. 150 Ma (Figure 5), indicating that they are formed by a contemporaneous magmatic event rather than residues of partial melting or xenoliths of the country rocks.

The magma mixing model is the most common and prevailing mechanism to interpret the origin of MEs in granites, especially in South China [6,7,61]. Generally, there are significant contrasts

of the chemical and isotopic compositions between MEs and the host granites derived from the mixing magma [62]. In our study, MEs and the host granites from the Xitian intrusion have a similar isotopic character. Previous studies suggested that similar chemical affinities are considered to be the consequence of the complete equilibration of dissimilar materials representing variable degrees of diffusive exchange between the felsic and more mafic magmas during slow cooling [8,63]. However, some results show that this isotopic equilibration can only be partially achieved. In some cases, highly mobile elements (especially alkali metal) equilibrate quickly than other elements [64]. So it is physically unlikely for isotopic ratios to be homogenized, whereas major and trace elements are not [65]. The Hf isotopic and O compositions of magmatic zircon grains from the MEs in the Xitian intrusion exhibit isotopic features similar to those of their host granites, requiring a common source or complete equilibration of dissimilar materials. In this situation, only mineral and textural evidence can be used to determine the processes whereby the MEs from the Xitian intrusion are formed.

The MEs are commonly darker than their host rocks in color and have a large volume of biotite. The textural relationship of porphyritic feldspar and MEs suggest the disequilibrium during melting (Figure 3g). Meanwhile, the features of the subhedral to allotriomorphic biotite and needle-like apatite, as observed in MEs from the Xitian intrusion, indicate a rapid cooling process. The similarity of enclaves with different colors in the Xitian intrusion suggests that they are probably formed from their host granites by kinetically induced, accelerated crystallization of ferromagnesian minerals, particularly biotite, related to rapid cooling [16]. All characters imply the MEs and their host granites were from the same parental magma rather than late isotope equilibrium, which excludes the magma mixing processes. Numerical models show that the granite magmas underwent a short period of chaotic convection and were generated in the upper cooling zone by melt-to-solid phase transformation [66]. These autoliths can be preserved in the chamber's upper and hotter interior and dragged downwards as descending convecting fingers. Such enclaves contain low-SiO<sub>2</sub> and high-temperature mineral phases [67,68], which are coincident with the MEs in Xitian (Supplementary Table S4).

## 6.2. Petrogenesis of the Xitian Intrusion

The Xitian host granites are devoid of a characteristic of Al-rich minerals (e.g., cordierite and muscovite) and have a slightly negative correlation between P<sub>2</sub>O<sub>5</sub> and SiO<sub>2</sub> (Figure 7), excluding S-type [69,70]. The weakly peraluminous feature of the Xitian host granites also precludes they are differentiated from a sedimentary source because this process would produce strongly peraluminous melts [71]. The host granites of the Xitian intrusion are high-K calc-alkaline rocks with much lower TFe<sub>2</sub>O<sub>3</sub>/MgO ratios (2.88–11.64) than the A-type granites (mean TFe<sub>2</sub>O<sub>3</sub>/MgO = 13.4). The temperature calculated by the geothermometer of Weston suggests that the cooling temperature of the Xitian granite (Mean = 781 °C, Supplementary Table S4) is lower than the temperature of typical A-type granite [72–74]. In contrast, all the above features of the Xitian intrusion suggest that the Xitian granite belongs to I-type, derived from dehydration melting of igneous rock or their metamorphic equivalents [75].

Both the host granites and the MEs display negative anomalies of Eu, Ba, Sr, Zr, P and Ti (Figure 8a). The decreasing trends of Al<sub>2</sub>O<sub>3</sub>, TiO<sub>2</sub>, and CaO with increasing SiO<sub>2</sub> for the Xitian host granites and the MEs are related to ilmenite, plagioclase, and biotite presence (Figure 7). It is worth noting that these chemical variations of host granites are in accordance with the crystal fractionation sequence of ferromagnesian minerals, plagioclase, Ti-Fe oxides, and apatite.

Garnet in the residue could result in substantial depletion of HREE in produced melts because of its extremely high partition coefficients for the HREE [76]. So the flat HREE patterns and higher HREE concentration may not be responsible for the entrapment of garnet in the residue. However, the hydrothermal process could justify the abundance of HREE [77]. Because of the physical and chemical properties, the content of rare earth elements in nature presents four groups of upper convex or lower concave curves [78]. According to the formula for quantitative analysis of the intensity of the four grouping effects proposed by [79], when  $t > 0$ , rare earth elements' distribution form presents the

four grouping effects. It can be concluded that the Xitian granite has an obvious four grouping effects (Figure 10). A lot of studies suggest that the four-group effect of rare earth elements in granite is the final result of rock-fluid interaction produced by highly evolved magma experiencing the separation of melt-fluid and fluid-gas [77,80]. It can be found that the late Jurassic Xitian pluton underwent magmatic crystallization and hydrothermal magmatism process.

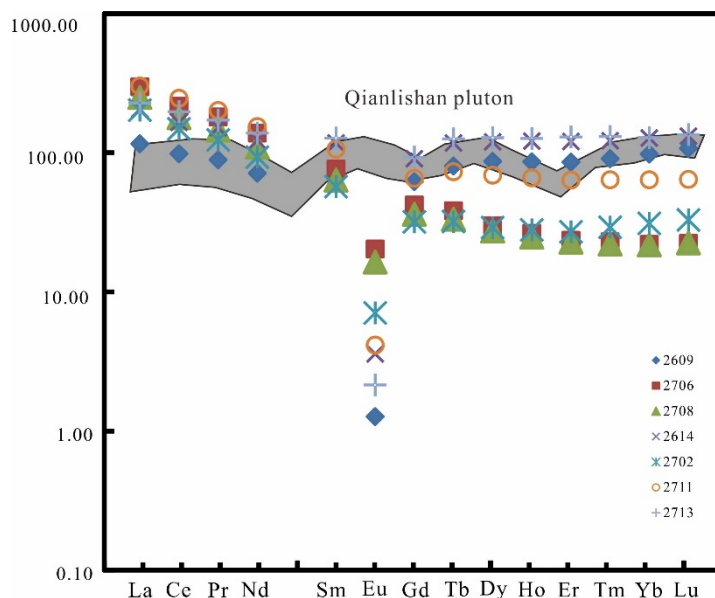


**Figure 10.** The four group effects of rare earth elements in the Xitian intrusion. The data of Qianlishan pluton are from [77].

In the process of magmatic evolution, granite can lead to a significant decrease in Cr, Ni, Sr, Ba, as well as a significant increase in the content of Li, Rb, and Cs [81]. Sr is mainly concentrated in magma’s early stage, while Rb is enriched in the residual melts. Therefore, Rb/Sr ratio is close to constant in the early stage of magma evolution, with an average value slightly less than 0.5 [82]. With the enhancement of differentiation, Rb/Sr ratio rapidly increases to more than 10, so Rb/Sr ratio can be used to represent the degree of differentiation. It can be found that both Nb/Ta and Zr/Hf ratios show a significant decrease with the increase of evolution degree (Figure 11).

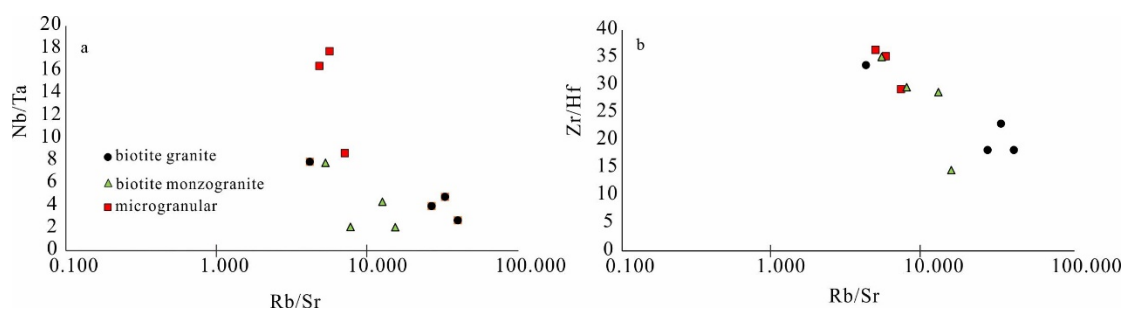


**Figure 11.** Variations of Rb/Sr versus Nb/Ta (a) and Zr/Hf (b) from the Xitian intrusion.

The variable range of Nb/Ta and Zr/Hf ratios are traditionally considered as the result from the separation and crystallization of accessory minerals containing these elements [83,84]. Rutile and ilmenite are essential carrier minerals of Nb and Ta. Since the  $D_{Nb/Ta}$  in rutile and ilmenite is less than 1, the separation and crystallization of rutile and ilmenite will decrease the Nb content and produce an elevated Nb/Ta ratio in the residual magma [85]. However, the Nb content in the late Jurassic

granite in the Xitian intrusion increases significantly with the increase of the degree of differentiation (Figure 11). It suggests that the separation and crystallization of Ti-rich minerals is not the reason for the Nb/Ta fractionation. A previous study has shown that the addition of fluid containing F will reduce the viscosity of magma and the temperature of the solid phase line, resulting in the increase of the solubility of Nb over Ta in silicate melts, Ta being less soluble [86]. Thus, the Nb and Ta contents will increase while the Nb/Ta ratio decrease (Figure 12). Some researchers summarized the Nb/Ta ratio of granite related to tungsten and tin mineralization and divided the petrogenesis of peraluminous granite into normal crystallization differentiation and magma-hydrothermal interaction by the index of Nb/Ta = 5 [87]. The majority of Nb/Ta ratio in the late Jurassic granite of the Xitian intrusion are below five, indicating the magma forming process was related to magmatic-hydrothermal processes (Supplementary Table S4).

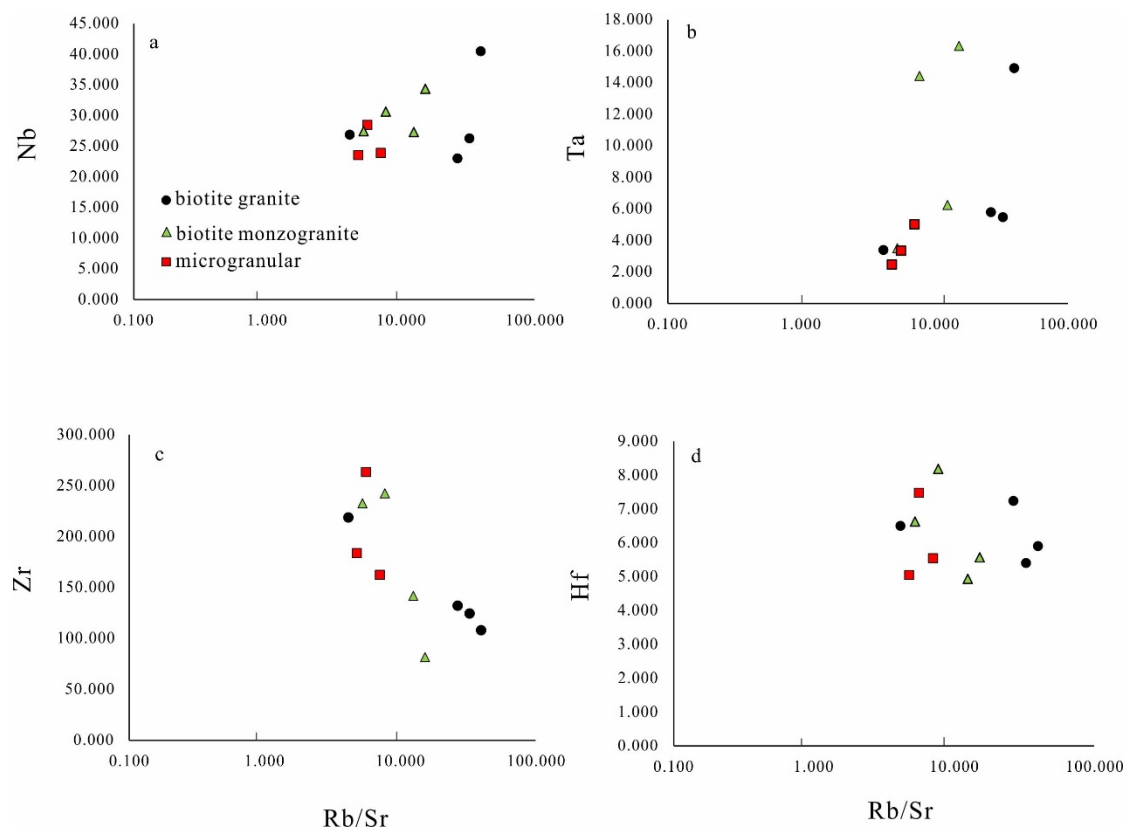


**Figure 12.** Variations of Rb/Sr versus the concentration of Nb (a), Ta (b), Zr (c), and Hf (d) from the Xitian intrusion.

Zircon is the main carrier mineral of Zr and Hf in granite. When magma reaches Zr saturation, it will crystallize zircon. Furthermore, because of the high Zr/Hf ratio (generally higher than 40) in zircon, the Zr/Hf ratio in the residual magma will significantly decrease after the separation and crystallization. However, the Zr/Hf ratio (Figure 11) and the Zr content in the Xitian intrusion decreased significantly with the increase of the degree of differentiation (Figure 12). Also, the Hf content of the Xitian late Jurassic granite did not decrease during the fractional process (Figure 12), which indicates that the variation of Zr/Hf ratio in the Xitian intrusion was not only due to the zircons crystallization. A previous study also showed that the Zr/Hf ratio, which decreases significantly with magmatic differentiation, is related to the magmatic system rich in F. It will increase the solubility of Zr and Hf, thus making Zr/Hf significantly differentiated [84].

### 6.3. Implications for Geodynamic Setting and Mineralization

As stated above, fractional crystallization implies effective separation of crystal and liquid fractions, which modifies the chemical equilibrium and enables magmatic differentiation. The separation of the early-crystallized minerals from melt would cause the residual magma to move upwards through buoyancy and being enriched in Si, Al, Na, K, and volatiles [88,89]. Calculations of melt density changes during fractionation show that compositional effects on density are usually greater than associated thermal effects [90]. The magma chamber in the middle crust is under large static pressure, where the volatiles can be highly dissolved in the residual magma [88]. The volatiles (F, Cl, CO<sub>2</sub>, etc.,) can decrease the solidus temperature of the silicate melt, prolonging the process of fractional crystallization [91]. Recent studies show that the injection of mafic magma into an early formed crystal-rich chamber would add heat and decrease magma viscosity, which can significantly promote the fractional crystallization process [92,93]. Mantle-derived mafic magmas are not necessary for direct material contributions to such a magma mixing but may provide a critical heat source for crustal melting [62].

Some researchers interpreted the Jurassic magmatism in South China as products due to the upwelling of the asthenosphere mantle, which is in response to the full-scale slab foundering and slab rollback [94]. According to the Pacific plate subduction model proposed by [94], the basalt layer in the lower middle crust of the Cathaysia block was probably closely related to the mantle upwelling in the asthenosphere caused by Pacific subduction during the Mesozoic [30]. After studied basalts of different ages in the South China plate, some scholars found that plate fragmentation occurred at 110–160 Ma, which caused disturbance of the asthenosphere and extensive magmatism in the Yanshan Period of South China, and large-scale polymetallic mineralization occurred in this period [95]. In our study, the existence of  $\epsilon_{\text{Hf}}(t)$  value above zero also suggests the involvement of the mantle component (Figure 13). Many researchers believe that fluids from the mantle are supercritical fluids, which are easy to form in subduction zones due to their characteristics of high temperature and high pressure, and are important media for element migration and mantle metasomatism in subduction zones [96,97]. With the upwelling of the asthenosphere mantle, the mantle-derived fluid could extract the metallogenic element efficiently [98,99]. Cavity expansion generates extreme reductions in pressure that cause the fluid to flow and expand the vapor. Such flash vaporization of the fluid results in the co-deposition of silica and metal elements [100].

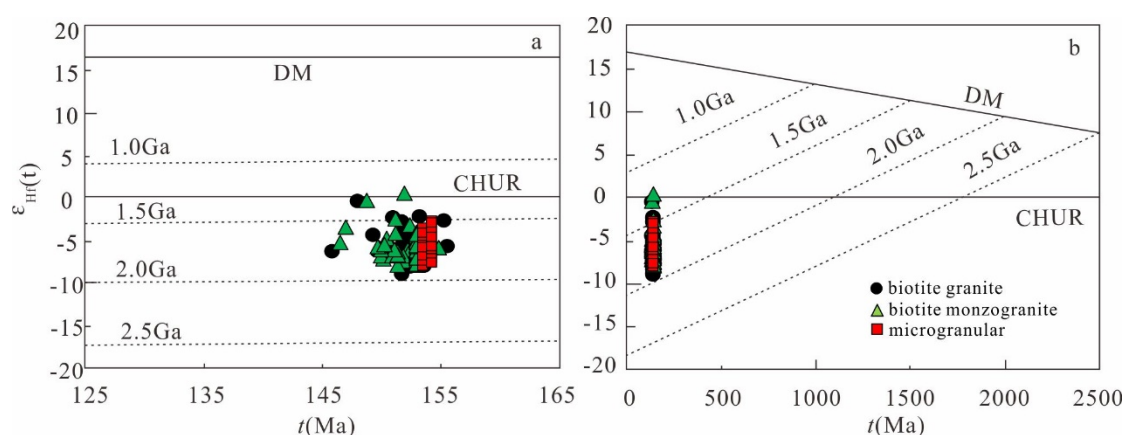


**Figure 13.** (a) U-Pb ages vs.  $\epsilon_{\text{Hf}}(t)$  diagram of zircon of the host granites and (b) MEs from the Xitian intrusion.

As shown in Figure 13, all the MEs samples plot below the CHUR reference line. Moreover, the host granites have similar  $\epsilon_{\text{Hf}}(t)$  values with the MEs and the zircon two-stage Hf model ages are similar to the Cathaysia Block [101]. These data provide additional support to the origin of the MEs and granites in the Xitian intrusion from a single isotopically homogeneous, lower crustal source.

Accordingly, given all these observations, we propose that the partial melting of the lower crust with mantle fluid resulted in the origin of the Xitian intrusion. It resulted from a change in the geodynamic regime, including break off/roll back of the subducted slab and subsequent regional extension.

## 7. Conclusions

A comprehensive study concerning the Late Jurassic Xitian intrusion and associated MEs provides evidence for the implication of geodynamic and mineralization in South China.

(1) MEs and their host granites are coeval and were emplaced at ca. 152 Ma.

(2) MEs were autoliths that experienced a period of chaotic convection and rapid cooling. Biotite granite and biotite monzogranite were generated from igneous sources, and they show evidence of volatiles addition.

(3) The mantle provides heat for crustal melting in our region. Separation and accumulation of evolved melts were facilitated by magma replenishment. It may result from the Pacific subduction.

**Supplementary Materials:** The following are available online at <http://www.mdpi.com/2075-163X/10/12/1059/s1>.

**Author Contributions:** Conceptualization, M.H. and Q.L.; Data curation, Q.L.; Formal analysis, M.H.; Funding acquisition, Q.H.; Investigation, M.H., Q.L., Q.H. and J.S.; Methodology, J.S.; Writing—original draft, M.H. writing—review and editing, Q.L. and Q.Y.; All authors have read and agreed to the published version of the manuscript.

**Funding:** This work was supported by the National Key R&D Program of China (2016YFC0600401), Public Welfare Project of the Ministry of land and Resources of China (201211024-04).

**Acknowledgments:** We thank Song G.X. and Zhang J.H. of the University of Chinese Academy of Sciences for assistance in major elements, trace elements, and zircon Hf-O isotope analyses. We thank Niurui at Henan Rock and Mineral Testing Center and Wu S.C., Zhu H.F. at 416 Brigade, Bureau of Geology and Mineral Exploration and Development of Hunan Province for their help with fieldwork.

**Conflicts of Interest:** The authors declare no conflict of interest.

## References

- Hu, R.Z.; Zhou, M.F. Multiple Mesozoic mineralization events in South China—An introduction to the thematic issue. *Miner. Depos.* **2012**, *47*, 579–588. [[CrossRef](#)]
- Mao, J.; Cheng, Y.; Chen, M.; Franco, P. Major types and time–space distribution of Mesozoic ore deposits in South China and their geodynamic settings. *Miner. Depos.* **2013**, *48*, 267–294.
- Zhao, W.W.; Zhou, M.F.; Li, Y.H.M.; Zhao, Z.; Gao, J.F. Genetic types, mineralization styles, and geodynamic settings of Mesozoic tungsten deposits in South China. *J. Asian Earth Sci.* **2017**, *137*, 109–140. [[CrossRef](#)]
- Chen, D.; Chen, Y.M.; Ma, A.J.; Liu, W.; Liu, Y.R.; Ni, Y.J. Magma mixing in the Xitian pluton of Hunan Province: Evidence from petrography, geochemistry and zircon U-Pb age. *Geol. China* **2013**, *41*, 61–78. (In Chinese with English Abstract)
- Shu, L.S.; Jahn, B.M.; Charvet, J.; Santosh, M.; Wang, B.; Xu, X.S.; Jiang, S.Y. Early Paleozoic depositional environment and intraplate tectono-magmatism in the Cathaysia Block (South China): Evidence from stratigraphic, structural, geochemical and geochronological investigations. *Am. J. Sci.* **2014**, *314*, 154–186. [[CrossRef](#)]
- Huang, X.D.; Lu, J.J.; Sizaret, S.; Wang, R.C.; Wu, J.W.; Ma, D.S. Reworked restite enclave: Petrographic and mineralogical constraints from the Tongshanling intrusion, Nanling Range, South China. *J. Asian Earth Sci.* **2018**, *166*, 1–18. [[CrossRef](#)]
- Xie, Y.C.; Lu, J.J.; Ma, D.S.; Zhang, R.Q.; Gao, J.F.; Yao, Y. Origin of granodiorite porphyry and mafic microgranular enclave in the Baoshan Pb-Zn polymetallic deposit, southern Hunan Province: Zircon U-Pb chronological, geochemical and Sr-Nd-Hf isotopic constraints. *Acta Petrol. Sin.* **2013**, *29*, 4186–4214. (In Chinese with English Abstract)
- Barbarin, B. Mafic magmatic enclaves and mafic rocks associated with some granitoids of the central Sierra Nevada batholith, California: Nature, origin, and relations with the hosts. *Lithos* **2005**, *80*, 155–177. [[CrossRef](#)]
- Didier, D.; Barbarin, B. *Enclaves and Granite Petrology, Development in Petrology*; Elsevier Science Publications: Amsterdam, The Netherlands, 1991; pp. 1–625.

10. Feeley, T.C.; Wilson, L.F.; Underwood, S.J. Distribution and compositions of magmatic inclusions in the Mount Helen dome, Lassen Volcanic Center, California: Insights into magma chamber processes. *Lithos* **2008**, *106*, 173–189. [[CrossRef](#)]
11. Burmakina, G.N.; Tsygankov, A.A. Mafic microgranular enclaves in late Paleozoic granitoids in the burgasy quartz syenite massif, Western Transbaikalia: Composition and petrogenesis. *Petrology* **2013**, *21*, 280–303. [[CrossRef](#)]
12. Tsygankov, A.A.; Khubanov, V.B.; Travin, A.V.; Lepekhina, E.N.; Burmakina, G.N.; Antsiferova, T.N.; Udoratina, O.V. Late Paleozoic gabbroids of western Transbaikalia: U-Pb and Ar-Ar isotopic ages, composition, and petrogenesis. *Russ. Geol. Geophys.* **2016**, *57*, 790–808. [[CrossRef](#)]
13. Chappell, B.W.; White, A.J.R.; Williams, I.S.; Wyborn, D.; Wyborn, L.A.I. Lachlan fold belt granites revisited: High- and low- temperature granites and their implications. *Aust. J. Earth Sci.* **2000**, *47*, 123–138. [[CrossRef](#)]
14. White, R.V.; Tarney, J.; Kerr, A.C.; Saunders, A.D.; Kempton, P.D.; Pringle, M.S.; Klaver, G.T. Modification of an oceanic plateau, Aruba, Dutch Caribbean: Implications for the generation of continental crust. *Lithos* **1999**, *46*, 43–68. [[CrossRef](#)]
15. Dahlquist, J.A. Mafic microgranular enclaves: Early segregation from metaluminous magma (Sierra de Chepes), Pampean Ranges, NW Argentina. *J. S. Am. Earth Sci.* **2002**, *15*, 643–655. [[CrossRef](#)]
16. Donaire, T.; Pascual, E.; Pin, C.; Duthou, J.L. Microgranular enclaves as evidence of rapid cooling in granitoid rocks: The case of the Los Pedroches granodiorite, Iberian Massif, Spain. *Contrib. Miner. Pet.* **2005**, *149*, 247–265. [[CrossRef](#)]
17. Shellnutt, J.G.; Jahn, B.M.; Dostal, J. Elemental and Sr–Nd isotope geochemistry of microgranular enclaves from peralkaline A-type granitic plutons of the Emeishan large igneous province, SW China. *Lithos* **2010**, *119*, 34–46. [[CrossRef](#)]
18. Flood, R.H.; Shaw, S.E. Microgranitoid enclaves in the felsic Looanga monzogranite, New England Batholith, Australia: Pressure quench cumulates. *Lithos* **2014**, *198*, 92–102. [[CrossRef](#)]
19. Clemens, J.D.; Gary, S.; Scott, E.B. Conditions during the formation of granitic magmas by crustal melting—Hot or cold; drenched, damp or dry? *Earth-Sci. Rev.* **2020**, *200*, 102982. [[CrossRef](#)]
20. Li, X.H. Cretaceous magmatism and lithospheric extension in Southeast China. *J. Asian Earth Sci.* **2000**, *18*, 293–305. [[CrossRef](#)]
21. Sun, W.D.; Ding, X.; Hu, Y.H.; Li, X.H. The golden transformation of the Cretaceous plate subduction in the west Pacific. *Earth Planet. Sci. Lett.* **2007**, *262*, 533–542. [[CrossRef](#)]
22. He, M.; Hou, Q.L.; Liu, Q.; Zhang, J.H.; Sun, J.F.; Wu, S.C.; Zhu, H.F. Timing and structural controls on skarn-type and vein-type mineralization at the Xitian tin-polymetallic deposit, Hunan Province, SE China. *Acta Geochim.* **2018**, *37*, 295–309. [[CrossRef](#)]
23. Liu, P.; Mao, J.W.; Santosh, M.; Bao, Z.A.; Zeng, X.J.; Jia, L.H. Geochronology and petrogenesis of the Early Cretaceous A-type granite from the Feie’shan W-Sn deposit in the eastern Guangdong Province, SE China: Implications for W-Sn mineralization and geodynamic setting. *Lithos* **2018**, *300*, 330–347. [[CrossRef](#)]
24. Zhou, Y.; Liang, X.; Wu, S.; Cai, Y.; Liang, X.; Shao, T.; Wang, C.; Fu, J.; Jiang, Y. Isotopic geochemistry, zircon U-Pb ages and Hf isotopes of A-type granites from the Xitian W-Sn deposit, SE China: Constraints on petrogenesis and tectonic significance. *J. Asian Earth Sci.* **2015**, *105*, 122–139. [[CrossRef](#)]
25. Li, H.; Yonezu, K.; Watanabe, K.; Tindell, T. Fluid origin and migration of the Huangshaping W-Mo polymetallic deposit, South China: Geochemistry and  $^{40}\text{Ar}/^{39}\text{Ar}$  geochronology of hydrothermal K-feldspars. *Ore Geol. Rev.* **2017**, *86*, 117–129. [[CrossRef](#)]
26. Cao, J.Y.; Wu, Q.H.; Yang, X.Y.; Kong, H.; Li, H.; Liu, B. Geochronology and genesis of the Xitian W-Sn polymetallic deposit in Eastern Hunan Province, South China: Evidence from zircon U-Pb and muscovite Ar–Ar dating, petrochemistry, and wolframite Sr–Nd–Pb isotopes. *Minerals* **2018**, *8*, 111. [[CrossRef](#)]
27. Zhao, W.W.; Zhou, M.F. In-situ LA-ICP-MS trace elemental analyses of magnetite: The Mesozoic Tengtie skarn Fe deposit in the Nanling Range, South China. *Ore Geol. Rev.* **2015**, *65*, 872–883. [[CrossRef](#)]
28. Zhou, X.M.; Sun, T.; Shen, W.Z.; Shu, L.S.; Niu, Y.L. Petrogenesis of Mesozoic granitoids and volcanic rocks in South China: A response to tectonic evolution. *Episodes* **2006**, *29*, 26–33. [[CrossRef](#)]
29. Yuan, S.D.; Mao, J.W.; Zhao, P.L.; Yuan, Y.B. Geochronology and petrogenesis of the Qibaoshan Cu-polymetallic deposit, northeastern Hunan Province: Implications for the metal source and metallogenic evolution of the intracontinental Qinhang Cu-polymetallic belt, South China. *Lithos* **2018**, *302–303*, 519–534. [[CrossRef](#)]

30. Yang, J.H.; Kang, L.F.; Peng, J.T.; Zhong, H.; Gao, J.F.; Liu, L. In-situ elemental and isotopic compositions of apatite and zircon from the Shuikoushan and Xihuashang granitic plutons: Implication for Jurassic granitoid-related Cu-Pb-Zn and W mineralization in the Nanling Range, South China. *Ore Geol. Rev.* **2018**, *93*, 382–403. [[CrossRef](#)]
31. Zhao, Z.; Liu, C.; Guo, N.X.; Zhao, W.W.; Wang, P.A.; Chen, Z.H. Temporal and spatial relationships of granitic magmatism and W mineralization: Insights from the Xingguo ore field, South China. *Ore Geol. Rev.* **2018**, *95*, 945–973. [[CrossRef](#)]
32. Niu, R.; Liu, Q.; Hou, Q.L.; Sun, J.F.; Wu, S.C.; Zhang, H.Y.; Guo, Q.Q.; Wang, Q. Zircon U-Pb geochronology of Xitian granitic pluton in Hunan Province and its constraints on the metallogenic ages of the tungsten-tin deposit. *Acta Petrol. Sin.* **2015**, *31*, 2620–2632. (In Chinese with English Abstract)
33. Fu, J.M.; Wu, S.C.; Xu, D.M.; Ma, L.Y.; Cheng, S.B.; Chen, X.Q. Reconstraint from zircon SHRIMP U-Pb dating on the age of magma intrusion and mineralization in Xitian Tungsten-tin polymetallic orefield, Eastern Province. *Geol. Miner. Resour. South China* **2009**, *3*, 1–7. (In Chinese with English Abstract)
34. Ma, T.Q.; Bai, D.Y.; Kuang, J.; Wang, X.H. Zircon SHRIMP dating of the Xitian granite pluton, Chanling, southeastern Hunan, and its geological significance. *Geol. Bull. China* **2005**, *24*, 415–419. (In Chinese with English Abstract)
35. Wu, Q.H.; Cao, J.Y.; Kong, H.; Shao, Y.J.; Li, H.; Xi, X.S.; Deng, X.T. Petrogenesis and tectonic setting of the early Mesozoic Xitian granitic pluton in the middle QinHang Belt, South China: Constraints from zircon U-Pb ages and bulk-rock trace element and Sr–Nd–Pb isotopic compositions. *J. Asian Earth Sci.* **2016**, *128*, 130–148. [[CrossRef](#)]
36. Liang, X.Q.; Dong, C.G.; Jiang, Y.; Wu, S.C.; Zhou, Y.; Zhu, H.F.; Fu, J.G.; Wang, C.; Shan, Y.H. Zircon U-Pb, molybdenite Re–Os and muscovite Ar–Ar isotopic dating of the Xitian W–Sn polymetallic deposit, eastern Hunan Province, South China and its geological significance. *Ore Geol. Rev.* **2016**, *78*, 85–100. [[CrossRef](#)]
37. Liu, B.; Li, H.; Wu, Q.H.; Kong, H.; Xi, X.S. Double-vein (ore-bearing vs. ore-free) structures in the Xitian ore field, South China: Implications for fluid evolution and mineral exploration. *Ore Geol. Rev.* **2019**, *115*, 103181. [[CrossRef](#)]
38. Liu, B.; Wu, Q.H.; Li, H.; Evans, N.J.; Wu, J.H.; Cao, J.Y.; Jiang, J.B. Fault-fluid evolution in the Xitian W–Sn ore field (South China): Constraints from scheelite texture and composition. *Ore Geol. Rev.* **2019**, *114*, 103140. [[CrossRef](#)]
39. Wei, W.; Song, C.; Hou, Q.L.; Chen, Y.; Faure, M.; Yan, Q.R.; Liu, Q.; Sun, J.F.; Zhu, H.F. The Late Jurassic extensional event in the central part of the South China Block—Evidence from the Laoshan’ao shear zone and Xiangdong Tungsten deposit (Hunan, SE China). *Int. Geol. Rev.* **2018**, *60*, 1644–1664. [[CrossRef](#)]
40. Sláma, J.; Košler, J.; Condon, D.J.; Crowley, J.L.; Gerdes, A.; Hanchar, J.M.; Horstwood, M.S.A.; Morris, G.A.; Nasdala, L.; Norberg, N.; et al. Plešovice zircon—A new natural reference material for U-Pb and Hf isotopic microanalysis. *Chem. Geol.* **2008**, *249*, 1–35. [[CrossRef](#)]
41. Li, X.H.; Liu, Y.; Li, Q.L.; Guo, C.H.; Chamberlain, K.R. Precise determination of Phanerozoic zircon Pb/Pb age by multicollector SIMS without external standardization. *Geochem. Geophys. Geosyst.* **2009**, *10*, Q04010.
42. Stacey, J.S.; Kramers, J.D. Approximation of terrestrial lead isotope evolution by a two-stage model. *Earth Planet. Sci. Lett.* **1975**, *26*, 207–221. [[CrossRef](#)]
43. Ludwig, K.R. *Users Manual for Isoplot/Ex Rev. 2.49*; Berkeley Geochronology Centre Special Publication: Berkeley, CA, USA, 2001; Volume 1, p. 56.
44. Xie, L.W.; Zhang, Y.B.; Zhang, H.H.; Sun, J.F.; Wu, F.Y. In situ simultaneous determination of trace elements, U-Pb and Lu-Hf isotopes in zircon and baddeleyite. *Chin. Sci. Bull.* **2008**, *53*, 1565–1573. [[CrossRef](#)]
45. Andersen, T. Correction of common lead in U-Pb analyses that do not report <sup>204</sup>Pb. *Chem. Geol.* **2002**, *192*, 59–79. [[CrossRef](#)]
46. Mandal, S.; Robinson, D.M.; Kohn, M.J.; Khanal, S.; Das, O.; Bose, S. Zircon U-Pb ages and Hf isotopes of the Askot klippe, Kumaun, northwest India: Implications for Paleoproterozoic tectonics, basin evolution and associated metallogeny of the northern Indian cratonic margin. *Tectonics* **2016**, *35*, 965–982. [[CrossRef](#)]
47. Gao, S.; Liu, X.M.; Yuan, H.L.; Hattendorf, B.; Gunther, D.; Chen, L.; Hu, S.H. Determination of forty two major and trace elements in USGS and NIST SRM glasses by laser ablation-inductively coupled plasma-mass spectrometry. *Geostand. Newsl.* **2002**, *26*, 181–196. [[CrossRef](#)]

48. Wu, F.Y.; Yang, Y.H.; Xie, L.W.; Yang, J.H.; Xu, P. Hf isotopic compositions of the standard zircons and baddeleyites used in U-Pb geochronology. *Chem. Geol.* **2006**, *234*, 105–126. [[CrossRef](#)]
49. Bouvier, A.; Vervoort, J.D.; Patchett, P.J. The Lu–Hf and Sm–Nd isotopic composition of CHUR: Constraints from unequilibrated chondrites and implications for the bulk composition of terrestrial planets. *Earth Planet. Sci. Lett.* **2008**, *273*, 48–57. [[CrossRef](#)]
50. Hoskin, P.W.O.; Ireland, T.R. Rare earth element chemistry of zircon and its use as a provenance indicator. *Geology* **2000**, *28*, 627. [[CrossRef](#)]
51. Rubatto, D.; Hermann, J. Zircon behavior deeply subducted rocks. *Elements* **2007**, *3*, 31–35. [[CrossRef](#)]
52. Rubatto, D. Zircon: The metamorphic mineral. *Rev. Mineral. Geochem.* **2017**, *83*, 261–295. [[CrossRef](#)]
53. Chappell, B.W.; White, A.J.R. Two contrasting granite types. *Pac. Geol.* **1974**, *8*, 173–174.
54. Peccerillo, A.; Taylor, S.R. Geochemistry of eocene calc-alkaline volcanic rocks from the Kastamonu area, Northern Turkey. *Contrib. Miner. Petrol.* **1976**, *58*, 63–81. [[CrossRef](#)]
55. Sun, S.S.; McDonough, W.F. Chemical and isotopic systematics of oceanic basalts: Implications for mantle composition and processes. In *Magmatism in the Ocean Basins*; Saunders, A.D., Norry, M.J., Eds.; Geological Society of London Special Publication: London, UK, 1989; Volume 42, pp. 313–345.
56. Griffin, W.L.; Wang, X.; Jackson, S.E.; Pearson, N.J.; O'Reilly, S.Y. Zircon geochemistry and magma mixing, SE China: In situ analysis of Hf isotopes, Tonglu and Pingtan igneous complexes. *Lithos* **2002**, *61*, 237–269. [[CrossRef](#)]
57. Clemens, J.D.; Elburg, M.A.; Harris, C. Origins of microgranular igneous enclaves in granitic rocks: The example of Central Victoria, Australia. *Contrib. Miner. Pet.* **2017**, *172*, 88. [[CrossRef](#)]
58. Schonenberger, J.; Marks, M.; Wagner, T.; Markl, G. Fluid-rock interaction in autoliths of agpaitic nepheline syenites in the Ilimaussaq intrusion, South Greenland. *Lithos* **2006**, *91*, 331–351. [[CrossRef](#)]
59. Pascual, E.; Donaire, T.; Pin, C. The significance of microgranular enclaves in assessing the magmatic evolution of a high-level composite batholith: A case on the Los Pedroches Batholith, Iberian Massif, Spain. *Geochem. J.* **2008**, *42*, 177–198. [[CrossRef](#)]
60. Barbarin, B.; Didier, J. Genesis and evolution of mafic microgranular enclaves through various types of interaction between coexisting felsic and mafic magmas. *Trans. R. Soc. Edinb. Earth Sci.* **1992**, *83*, 145–153.
61. Chen, Y.; Song, S.; Niu, Y.; Wei, C. Melting of continental crust during subduction initiation: A case study from the Chaidanuo peraluminous granite in the North Qilian suture zone. *Geochim. Cosmochim. Acta* **2014**, *132*, 311–336. [[CrossRef](#)]
62. Clemens, J.D.; Regmi, K.; Nicholls, I.A.; Weinberg, R.; Maas, R. The Tynong pluton, its mafic synplutonic sheets and igneous microgranular enclaves: The nature of the mantle connection in I-type granitic magmas. *Contrib. Miner. Pet.* **2016**, *171*, 35. [[CrossRef](#)]
63. Tod, E.; Waight, R.M.; Ian, A.N. Geochemical investigations of microgranitoid enclaves in the S-type Cowra Granodiorite, Lachlan Fold Belt, SE Australia. *Lithos* **2001**, *56*, 165–186.
64. Johnston, A.D.; Wyllie, P.J. Interaction of granitic and basic magmas: Experimental observations on contamination processes at 10 kbar with H<sub>2</sub>O. *Contrib. Miner. Petrol.* **1988**, *98*, 352–362. [[CrossRef](#)]
65. Niu, Y.L.; Zhao, Z.D.; Zhu, D.C.; Mo, X.X. Continental collision zones are primary sites for net continental crust growth—A testable hypothesis. *Earth-Sci. Rev.* **2013**, *127*, 96–110. [[CrossRef](#)]
66. Bea, F. CrySTALLIZATION dynamics of granite magma chambers in the absence of regional stress: Multiphysics modeling with natural examples. *J. Petrol.* **2010**, *51*, 1541–1569. [[CrossRef](#)]
67. Cambese, A.; Montero, P.; Molina, J.F.; Hyppolito, T.; Bea, F. Constraints of mantle and crustal sources and interaction during orogenesis: A zircon SHRIMP U-Th-Pb and O isotope study of the ‘cal-alkaline’ Brovales pluton, Ossa-Morena Zone, Iberian Variscan Belt. *Lithos* **2019**, *324–325*, 661–683. [[CrossRef](#)]
68. Moita, P.; Santos, J.F.; Pereira, M.F.; Costa, M.M.; Corfu, F. The quartz-dioritic Hospitais intrusion (SW Iberian Massif) and its mafic microgranular enclaves—Evidence for mineral clustering. *Lithos* **2015**, *224–225*, 78–100. [[CrossRef](#)]
69. Chappell, B.W. Aluminium saturation in I- and S-type granites and the characterization of fractionated haplogranites. *Lithos* **1999**, *46*, 535–551. [[CrossRef](#)]
70. Wu, F.Y.; Jahn, B.; Wilde, S.A.; Lo, C.H.; Yui, T.F.; Lin, Q.; Ge, W.C.; Sun, D.Y. Highly fractionated I-type granites in NE China (I): Geochronology and petrogenesis. *Lithos* **2003**, *66*, 241–273. [[CrossRef](#)]

71. Douce, A.E.P.; Johnston, A.D. Phase equilibria and melt productivity in the polytic system: Implications for the origin of peraluminous granitoids and aluminous granulites. *Contrib. Miner. Petrol.* **1991**, *107*, 202–218. [[CrossRef](#)]
72. Waston, E.B.; Harrison, T.M. Zircon saturation revisited—temperature and composition effects in a variety of crustal magma types. *Earth Planet. Sci. Lett.* **1983**, *64*, 295–304.
73. Clemens, J.D.; Holloway, J.R.; White, A.J.R. Origin of an A-type granite: Experimental constraints. *Am. Mineral.* **1986**, *71*, 317–324.
74. King, P.L.; Chappell, B.W.; Allen, C.M.; White, A.J.R. Are A-type granite the high-temperature felsic granites? Evidence for fractionated granites of the Wangrah Suite. *Aust. J. Earth Sci.* **2001**, *48*, 501–514. [[CrossRef](#)]
75. Wolf, M.B.; Wyllie, P.J. Dehydration-melting of amphibolite at 10 kbar: The effects of temperature and time. *Contrib. Miner. Petrol.* **1994**, *115*, 369–383. [[CrossRef](#)]
76. Bea, F. Residence of REE, Y, Th and U in granites and crustal protoliths; Implications for the chemistry of crustal melts. *J. Petrol.* **1996**, *37*, 521–552. [[CrossRef](#)]
77. Tao, J.; Li, W.; Li, X.; Cen, T. Petrogenesis of early Yanshanian highly evolved granites in the Longyuanba area, southern Jiangxi Province: Evidence from zircon U-Pb dating, Hf-O isotope and whole-rock geochemistry. *Sci. China Earth Sci.* **2013**, *56*, 922–939. [[CrossRef](#)]
78. Zhao, Z.H.; Masuda, A. REE evidence for water-rock interaction in tin/tungsten granites. In *Fifth International Symposium on Tin/Tungsten Granites in Southeast Asia and the Western Pacific*; Shimane University: Matsue, Japan, 1988; pp. 257–258.
79. Monecke, T.; Kempe, U.; Monecke, J.; Sala, M.; Wolf, D. Tetrad effect in rare earth element distribution patterns: A method of quantification with application to rock and mineral samples from granite-related rare metal deposits. *Geochim. Cosmochim. Acta* **2002**, *66*, 1185–1196. [[CrossRef](#)]
80. Zhao, Z.; Bao, Z.; Qiao, Y. A peculiar composite M- and W-type REE tetrad effect: Evidence from the Shuiquangou alkaline syenite complex, Hebei Province, China. *Chin. Sci. Bull.* **2010**, *55*, 2684–2696. [[CrossRef](#)]
81. Gelman, S.E.; Deering, C.D.; Bachmann, O.; Huber, C.; Gutiérrez, F.J. Identifying the crystal graveyards remaining after large silicic eruptions. *Earth Planet. Sci. Lett.* **2014**, *403*, 299–306. [[CrossRef](#)]
82. Nockolds, S.R.; Allen, R. The geochemistry of some igneous rock series. *Geochim. Cosmochim. Acta* **1953**, *4*, 105–142. [[CrossRef](#)]
83. Linnen, R.L.; Keppler, H. Columbite solubility in granitic melts: Consequences for the enrichment and fractionation of Nb and Ta in the Earth's crust. *Contrib. Miner. Petrol.* **1997**, *128*, 213–227. [[CrossRef](#)]
84. Linnen, R.L.; Keppler, H. Melt composition control of Zr/Hf fractionation in magmatic processes. *Geochim. Cosmochim. Acta* **2002**, *66*, 3293–3301. [[CrossRef](#)]
85. Pfander, J.A.; Munker, C.; Stracke, A.; Mezger, K. Nb/Ta and Zr/Hf in ocean island basalts—Implications for crust-mantle differentiation and the fate of Niobium. *Earth Planet. Sci. Lett.* **2007**, *254*, 158–172. [[CrossRef](#)]
86. Zarausky, G.P.; Korzhinskaya, V.; Kotova, N. Experimental studies of Ta<sub>2</sub>O<sub>5</sub> and columbite–tantallite solubility in fluoride solutions from 300 to 550 °C and 50 to 100 MPa. *Mineral. Petrol.* **2010**, *99*, 287–300. [[CrossRef](#)]
87. Ballouard, C.; Poujol, M.; Boulvais, P.; Branquet, Y.; Tartèse, R.; Vigneresse, J.L. Nb-Ta fractionation in peraluminous granites: A marker of the magmatic-hydrothermal transition. *Geology* **2016**, *44*, 231–234. [[CrossRef](#)]
88. Sparks, R.S.J.; Huppert, H.E. Density changes during the fractional crystallization of basaltic magmas: Fluid dynamic implications. *Contrib. Miner. Petrol.* **1984**, *85*, 300–309. [[CrossRef](#)]
89. Hildreth, W. The timing of caldera collapse at Mount Katmai in response to magma withdrawal toward Novarupta. *Geophys. Res. Lett.* **1991**, *18*, 1541–1544. [[CrossRef](#)]
90. Balcone-Boissard, H.; Villemant, B.; Boudon, G.; Michel, A. Halogen behaviours during andesitic magma degassing: From magma chamber to volcanic plume. *EGU Gen. Assem.* **2009**, *11*, 11985.
91. Veksler, I.V.; Dorfman, A.M.; Dulski, P.; Kamensky, V.S.; Danyushevsky, L.V.; Jeffries, T.; Dingwell, D.B. Partitioning of elements between silicate melt and immiscible fluoride, chloride, carbonate, phosphate and sulfate melts, with implications to the origin of natrocarbonatite. *Geochim. Cosmochim. Acta* **2012**, *79*, 20–40. [[CrossRef](#)]
92. Bachmann, O. On the origin of crystal-poor rhyolites: Extracted from batholithic crystal mushes. *J. Petrol.* **2004**, *45*, 1565–1582. [[CrossRef](#)]

93. Bachmann, O.; Huber, C. Silicic magma reservoirs in the Earth's crust. *Am. Mineral.* **2016**, *101*, 2377–2404. [[CrossRef](#)]
94. Li, Z.X.; Li, X.H. Formation of the 1300-km-wide intracontinental orogen and postorogenic magmatic province in Mesozoic South China: A flat-slab subduction model. *Geology* **2007**, *35*, 179–182. [[CrossRef](#)]
95. Meng, L.F.; Li, Z.X.; Chen, H.L.; Li, X.H.; Wang, X.C. Geochronological and geochemical results from Mesozoic basalts in southern South China Block support the flat-slab subduction model. *Lithos* **2012**, *132–133*, 127–140. [[CrossRef](#)]
96. Deschamps, F.; Godard, M.; Guillot, S.; Hattori, K. Geochemistry of subduction zone serpentinites: A review. *Lithos* **2013**, *178*, 96–127. [[CrossRef](#)]
97. Spandler, C.; Pirard, C. Element recycling from subducting slabs to arc crust: A review. *Lithos* **2013**, *170*, 208–223. [[CrossRef](#)]
98. Shervais, J.W.; Jean, M.M. Inside the subduction factory: Modeling fluid mobile element enrichment in the mantle wedge above a subduction zone. *Geochim. Cosmochim. Acta* **2012**, *95*, 270–285. [[CrossRef](#)]
99. Liu, X.; Li, C.; Lu, Q.; Deng, B.; Song, X.; Zhao, F.; Chu, Y.; Xiao, J.; Yi, L.; Huang, Y. The genesis mechanism of the mantle fluid action and evolution in the ore-forming process: A case study of the Laowangzhai gold deposit in Yunnan, China. *Acta Geol. Sin. (Engl. Ed.)* **2012**, *86*, 608–618.
100. Weatherley, D.K.; Henley, R.W. Flash vaporization during earthquakes evidenced by gold deposits. *Nat. Geosci.* **2013**, *6*, 294–298. [[CrossRef](#)]
101. Yu, J.H.; O'Reilly, Y.S.; Wang, L.J.; Griffin, W.L.; Zhou, M.F.; Zhang, M.; Shu, L.S. Components and episodic growth of Precambrian crust in Cathaysia Block, South China: Evidence from U-Pb ages and Hf isotopes of zircons in Neoproterozoic sediments. *Precambrian Res.* **2010**, *181*, 97–114. [[CrossRef](#)]

**Publisher's Note:** MDPI stays neutral with regard to jurisdictional claims in published maps and institutional affiliations.



© 2020 by the authors. Licensee MDPI, Basel, Switzerland. This article is an open access article distributed under the terms and conditions of the Creative Commons Attribution (CC BY) license (<http://creativecommons.org/licenses/by/4.0/>).